DOI: https://doi.org/10.37434/tpwj2024.11.01

MECHANICAL AND THERMAL BEHAVIOR OF ADDITIVELY MANUFACTURED Invar 36 USING A LASER HOT WIRE HYBRID DED PROCESS

Bharat Yelamanchi[1], Andrew Prokop[1], Coleman Buchanan[1], Aayush Alok[1], Mario Rodriguez[2], Jimena Morales[2], Holly Martin[1], Brian Vuksanovich[1], Virgil Solomon[1], Eric MacDonald[2], Yousub Lee[3], Thomas Feldhausen[2,4], Pedro Cortes[2]

[1]Youngstown State University, OH USA 44555
[2]College of Engineering, The University of Texas at El Paso, TX USA 79968
[3]Computational Sciences & Engineering Division, Oak Ridge National Laboratory, TN, USA
[4]Manufacturing Science Division, Oak Ridge National Laboratory, TN, USA

ABSTRACT

Invar 36 alloy is a material of high interest in the composite tooling sector due to its low coefficient of thermal expansion. Current production of Invar 36 tooling using traditional manufacturing such as casting and forging is associated with long lead times due to a multitude of factors such as labor and component shortages, high material costs, foreign competition, and supply chain issues. An attractive alternate process is the use of an integrated 5-axis CNC hybrid Laser Hot Wire Deposition System (LHWD) for manufacturing invar molds. The hybrid process provides a combination of the additive and subtractive technologies resulting in a synergistic platform for producing and repairing structures and molds. The main novelty and goal of this work is to study the properties of Invar deposited by a LHWD and to provide guidelines for the manufacture of parts using this process. In this study, the thermal expansion behavior of the manufactured specimens has been analyzed and related to its printing parameters and direction. Multiple specimens were extracted for mechanical, dilatometry and metallographic testing. A thermal IR recording of the printing process was also carried out to observe the thermal history of the produced parts to establish thermal influence on performance-property-processing relationship. The results of these tests show the advantage of LHWD technology for the manufacture of Invar alloy parts, as it presents similar thermal expansion behavior as those commercially available with minimal presence of precipitates and no macrostructural failures such as pores, cracks and lacks of fusion.

KEYWORDS: hybrid directed energy deposition, Invar, hybrid manufacturing, additive manufacturing, subtractive manufacturing, wire and laser additive manufacturing (WLAM), directed energy deposition (DED), laser hot-wire deposition (LHWD)

INTRODUCTION

Invar alloys, since their discovery have been a widely used material in precision measurement applications and other applications such as pendulums for clocks and thermostats because of their unusual physical behavior of no thermal expansion with temperature change. This phenomenon has been observed in Fe–Ni alloys with Ni concentrations within a range of 30–45 % [1]. Nowadays, the applications of Invar alloys are very diverse including satellite, metrology, LNG carrier, precision instruments, dies, TV kinescopes, liquid natural gas and cryogenic tanks, as well as orbiting satellites, and aerospace tooling [2–6]. Invar stands out because of its low Coefficient of Thermal Expansion (CTE), or its lack of expansion or contraction with changes in temperature [7, 8]. The material of choice in this study, Invar 36, is within this range with a composition in weight of 64 % Fe and 36 % Ni, and a CTE value below $2 \cdot 10^{-6}$ K^{-1} at room temperature [9].

With Fe having a BCC structure, Fe–Ni alloy combined with a concentration higher than 30 % of Ni with FCC structure, the alloy tends to be weldable with an austenitic FCC structure, where Ni is the γ stabilizer of iron. The Curie temperature (T_c) of wrought Invar 36 is 279 °C and so it shows a very low CTE and ferromagnetic properties below this temperature [10]. Above T_c, the material is paramagnetic with the thermal expansion behavior similar to other metals such as Fe. T_c peaks at a Ni concentration of approximately 66 % and decreases when the Ni concentration drops lower than 40 % due to a reduction in permeability [11]. On the other hand, Invar with its austenitic structure is also hard to machine because of its high ductility, work hardening and low conductivity [12, 13]. Nevertheless, they are adequate for welding [14, 15]. Therefore, hybrid manufacturing, a combination of additive and subtractive processes within the same machine is a good alternative to traditional techniques for the manufacturing of Invar parts, because these technologies are able to manufacture near net shape geometry without large amounts of machining needed.

In the previous works, mostly Laser Powder Bed Fusion (LPBF) technique was employed to exhaustively analyze the evaluation of the CTE value and Curie temperature in materials processed by additive techniques [16–20]. Asgari et al [21] in their study manufactured Invar samples with Fe–Ni (36 %) with SLM technology utilizing different process parameters with significance to laser power. After performing X-ray computed

tomography (CT) to look at the microstructure, density, structural integrity (determining pore size, morphology and inter-alignment of pores), chemical composition and thermal expansion behavior of the manufactured samples, it was concluded that sample densities were higher than 99.8 % in all cases, and the porosity level decreased at higher laser powers.

Yakout et al. [22] reported that the CTE value is related to the volumetric energy density of SLM technology. In the SLM process, the volumetric energy density (J/mm^3) is calculated as the ratio between laser power (W) and the multiplication between the average scanning speed (mm/s), hatch spacing (mm) and layer thickness (mm). It was found that there is a critical laser energy density (identified as 86.8 J/mm^3), for which the SLM process is optimal in terms of material properties. This critical energy density achieves stable melting with a homogeneous composition and microstructure, magnetic properties and similar CTE to those obtained in the commercially available material.

Below the critical energy, the manufactured samples exhibited no significant changes in composition, although voids (gas pores or lack of fusion) formed, and the CTE decreased. In contrast, above this critical energy, the number of voids decreased, but the composition of the samples changed: nickel and manganese levels decreased, while iron, molybdenum, and silicon levels increased. This rise in silicon and molybdenum resulted in a further reduction in CTE and an increase in the magnetic moment of the part [23]. Wegener et al [9] manufactured samples using the SLM process with CTE values of $1.8 \cdot 10^{-6}$ K^{-1} between 0 and 100 °C that were similar to the values of conventionally processed materials. Moreover, adjusting the processing parameters of the LMD process, which employs a 4 kW CO_2 laser and a four-tip coaxial nozzle, resulted in CTE values comparable to those obtained with conventional processing methods [24]. Huang et al [16] fabricated test specimens in multiple orientations and observed that there is significant anisotropy in the microstructure of Invar 36 and hence the mechanical properties. In the same study, they observed that the CTE of Invar 36 alloy in 0°, 45°, and 90° orientation at 30 ~ 200 °C are $1.78 \cdot 10^{-6}$ °C^{-1}, $1.62 \cdot 10^{-6}$ °C^{-1} and $1.77 \cdot 10^{-6}$ °C^{-1}, respectively, meeting ASTM F1686 standards. Huang et al [25] in another study on additive manufacturing of Invar alloy have identified that even though acceptable mechanical properties and CTE were achieved using the LPBF technology, further optimization is required to understand and resolve the anisotropy based on build orientation. Finally, as was mentioned above, in the previous literature, even though many studies were conducted on additive manufacturing Invar36 alloy using LPBF, few studies have been carried out analyzing the microstructures and the mechanical properties of Invar parts manufactured using WAAM technology and, therefore there is a lack of study on its resulting mechanical and thermal properties.

In this paper, mechanical and thermal expansion properties displayed by Invar specimens manufactured using the LHWD system were analyzed and compared with commercially available Invar 36. This study was implemented with the aim of validating the LHWD technology as a reliable method for manufacturing Invar 36 parts for tooling applications in the aerospace and automotive sectors.

EXPERIMENTAL METHODS AND METHODOLOGY

Fabrication of the test specimen was performed using a Mazak VC500A/5X AM hot wire deposition (HWD) system. A bead analysis was conducted in order to establish a baseline process parameter set for printing the parts. Two different bulk geometries, cube and cuboid were printed using the laser hot wire deposition system in the Bidirectional 0° (Bi0), Bidirectional rotation positive 45° (BRP45) and Bidirectional rotation positive 90° (BRP90) orientation as shown in Figure 1. Following the printing process, the bulk geometries were machined to a net shape in *X* and *Y* dimensions of the tensile, CTE, and hardness samples as shown in Figure 2.

These were then detached from the base and cut to the required *XYZ* dimensions using a wire Electrical Discharge Machining (EDM). Samples were taken from the top, middle and bottom zones of the multilayered print also shown in Figure 1, *a* 1.14 mm (0.045″) diameter Invar 36 wire from Arcos Industries, LLC, was used to fabricate the component. Argon was used as a local shielding gas with a volumetric flow rate of 30 L per minute. The produced dog-bone tensile samples conform to the ASTM E8/E8M-16a standard for tension testing of metallic materials. The cylindrical hardness samples conform to ASTM E18-15 standard for performing rockwell hardness testing. CTE samples conform to ASTM E831-19. A control was also tested with the aforementioned tests on the stock materials ordered from Mcmaster Carr.

This study employed two machining sequences. The first sequence involved a subtractive process that utilized the hybrid manufacturing capabilities of the unit to machine the rough edges created by excess deposition during the printing stage. Here, the subtracting process was performed on the samples once they have reached room temperature. The second sequence consisted of using an EDM to cut the parts off the build platform and to the final dimensions in line with the ASTM's corresponding to the respective test methods. Because of the smaller sizes of the final parts compared to what can be achieved with the mounted tools on the Hybrid system, the EDM method was employed to have better control on the subtractive process. Hyper-

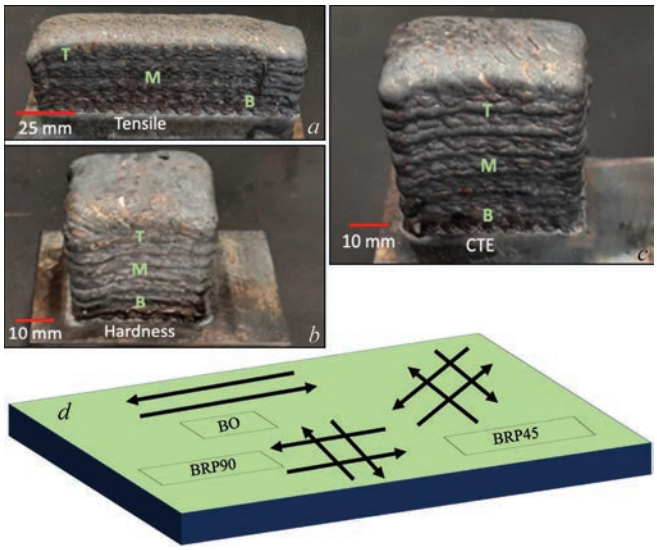

Figure 1. Bulk specimens as printed: *a* — tensile; *b* — hardness; *c* — CTE, and *d* — schematic of the B0, BRP45 and BRP90 print orientations of the manufactured bulk specimens. Positive rotation indicates a clockwise direction

Mill, a computer aided manufacturing (CAM) software from Open mind technologies was used to program the toolpath trajectory for the deposition and first machining sequence. This program accepts the nominal CAD geometry and creates g-code for the developed toolpath trajectories. Builds with three different orientations namely unidirectional, bidirectional, and 90° angle were fabricated and tested in this study.

MECHANICAL AND DILATOMETRY TESTING

To identify the mechanical performance of the parts printed using the VC500A/5X, tensile and hardness tests were conducted. The tensile tests were performed on an Instron in compliance with ASTM E8 subsize specimen. A 150 kN load cell was used to gather the load information and an extensometer was used to gather reliable strain information. Ultimate tensile strength, young's modulus and strain at failure were calculated from the load-extension and strain data obtained from the testing. The Rockwell hardness tests were conducted using a type B spherical indenter in compliance with ASTM E18. The CTE tests were conducted on TA Instruments (Delaware) TMA-Q400 based on ASTM E831-19. In this test, the linear deflection of the sample was measured, and the CTE (10^{-6} um/m·°C^{-1}) was calculated following Eq. (1):

$$\mathrm{CTE} = \alpha = \Delta L / \left(L_0 \Delta T\right), \tag{1}$$

where ΔL is the linear deflection; L_0 is the initial length of the samples and ΔT the temperature difference for which ΔL is measured.

MICROSTRUCTURE ANALYSIS

As-printed samples have been prepared for microstructural, chemical, and crystallographic investigations using metallographic techniques. The crystallographic investigations were performed by X-ray diffraction (XRD) using a Rigaku Miniflex II XRD equipped with a Cu X-ray source. The microstructural investigations were performed using light and electron microscopy techniques. The Optical microscopy investigation was carried out using a Keyence VHX-7000 Digital Microscope. The electron microscopy investigations were performed using a JEOL JSM-7600F scanning electron microscope (SEM) equipped with an EDAX Apollo XV X-ray energy dispersive spectrometer (EDS) for chemical analysis.

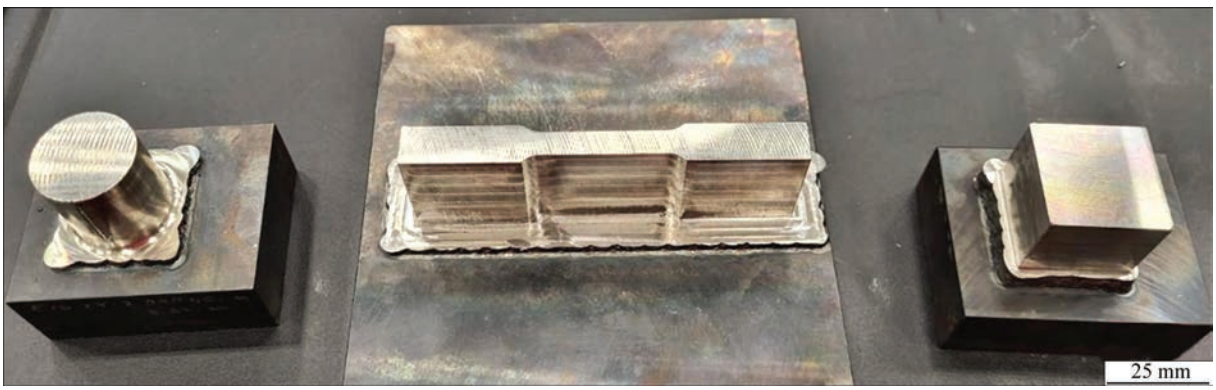

Figure 2. Machined part geometries for: *a* — hardness; *b* — tensile, and *c* — CTE tests

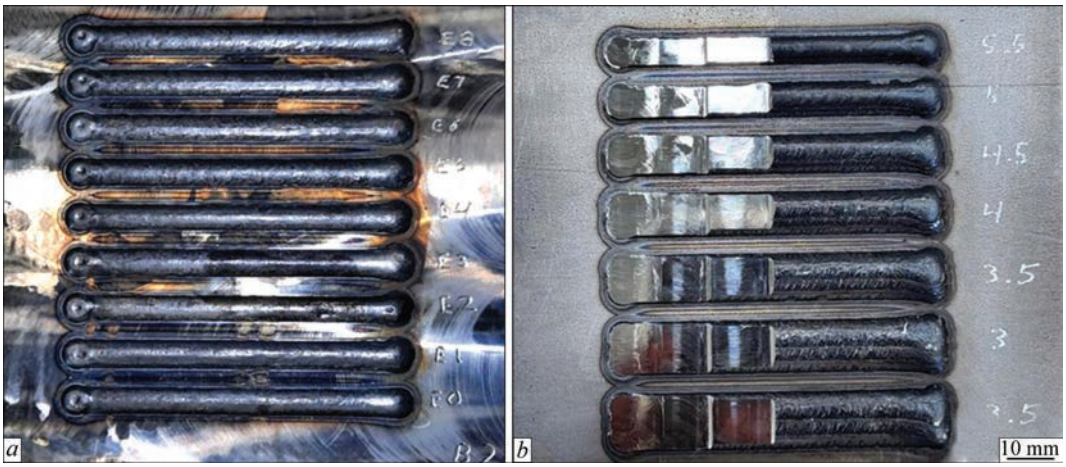

Figure 3. Beads deposited with the process parameter sets E0–E8 (*a*) and overstep analysis (*b*)

THERMAL ANALYSIS

Thermal imaging was employed to monitor the process dynamics of the Laser Hot Wire Deposition of the Invar 36 samples. A FLIR A655sc LWIR camera with f/1.0 and a field of view of 15°×11° (19° diagonal) capable of detecting and converting the emitted InfraRed radiation to temperatures range of –15 to 2000 °C was used. Images were acquired at a resolution of 640×480 pixels at 6 fps. The raw 32-bit data was converted to 16-bit arrays for computational efficiency. Custom Python scripts were developed utilizing the FLIR SDK library for image analysis and video processing. This enabled specialized cropping and data extraction. To extract temperature data, a 10×10-pixel averaging approach was applied to calculate mean temperatures at different heights (lower, middle, upper) of the build. This method was selected since it provides representative data from the desired layer within the printed part.

Table 1. Build process parameter development

Parameter set	Feed rate during deposition, mm/min	Laser power, W	Shielding gas, L/min	Wire feed speed, mm/min	Hot wire power, W
E0 (control)	792	3510	10	4191	480
E1	500	3510	10	4191	480
E2	1200	3510	10	4191	480
E3	792	4000	10	4191	480
E4	792	3200	10	4191	480
E5	792	3510	10	5207	480
E6	792	3510	10	3175	480
E7	792	3510	10	4191	600
E8	792	3510	10	4191	360
Final printing	792	3510	30	4191	600

RESULTS AND DISCUSSION

PRINTING PARAMETER DEVELOPMENT

A comprehensive bead analysis was initially carried out in the 0° orientation before fabricating the parts to understand the influence of process parameters and printing direction on the quality. It was observed that five process parameters dictate the printability. These being the traverse feed rate during deposition, laser power, shielding gas, wire feed speed and hot wire power. In addition to these parameters, there were two toolpath parameters namely Step over and Layer height, specified in Hypermill software, that define the quality of the build when combined with the other five aforementioned process parameters. With a target bead height of around 2.1 mm, and a bead width of 6.5 mm, a total of eight different process parameter sets were investigated in the bead analysis to define the printability based on the initial feedback from the manufacturer of the machine. These parameters are as shown in Table 1.

The beads deposited using the printing parameter sets mentioned in Table 1 are as shown in Figure 3, *a*. It was observed that all parameter sets resulted in a weld bead with consistent thickness, width and height except for E2. Signs of starvation were observed in the weld bead deposited with the parameter set E2. This is because the feed rate of deposition, which is the rate at which the printing head moves, is increased to 1200 from 500 mm/min without making any changes in the wire feed speed.

Upon closer observation of the other beads, it was observed that the parameter set E0 produced a good quality bead with the required height but not the width. E1 resulted in a bead that is too tall because of slowing down the Feed rate of deposition from 792 to 500 mm/min while the wire is being feeded to the system at 4191 mm/min. E3, E5, E6 and E8 resulted in flatter and wider beads due to the higher laser power which results in the larger heat affected zone of the substrate, higher wire feed speed which results in expansion of the weld pool region and insufficient preheating of the

wire which would result in a condition similar to starvation if a proper wire feed rate is not maintained. The dimensions of the individual beads are as specified in Table 2. E4 and E7 resulted in the beads closest to the requirement. A quick overlap analysis was also conducted as shown in Figure 3, *b* in order to obtain the ideal stepover during deposition which will preserve the required build conditions. Upon dimension analysis, a stepover of 2.5 mm was decided to be ideal as it produces a layer height of 2.1 mm during print with the final printing parameter set mentioned in Table 1. All the other overlap conditions resulted in taller beads which would result in taller layer height.

Table 2. Bead analysis parameters and their corresponding bead dimensions

Parameter set	Bead width, mm	Bead height, mm
E0	6.21 ± 0.40	1.54 ± 0.30
E1	6.53 ± 0.40	2.24 ± 0.20
E2	6.26 ± 0.80	1.04 ± 0.19
E3	6.75 ± 1.10	1.27 ± 0.01
E4	6.32 ± 0.60	1.49 ± 0.07
E5	6.66 ± 0.60	1.03 ± 0.14
E6	6.56 ± 0.50	1.22 ± 0.11
E7	6.66 ± 1.00	1.45 ± 0.14
E8	6.66 ± 0.60	1.38 ± 0.08

THERMAL ANALYSIS

The heat input and the temperature gradients during the deposition and the waiting time of a single bead manufactured using LHWD observed using a IR camera can be observed in Figure 4. Top, middle, and bottom zones were selected for the IR analysis in order to obtain a complete understanding of the thermal history involved in the manufacturing of the part. The heat input is a critical condition that affects the CTE of the material.

By capturing and graphing the temperature profiles of the three layers, a general trend in thermal histories related to the build height was identified. The bottom section, connected to a large thermally conductive build plate, released heat rapidly, resulting in minimal heat accumulation. Figure 4 displays the cooling process on the initial layers, where the temperature drop can be observed. This process can lead to relatively small crystal grains, resulting in enhanced mechanical performance. As additional layers are added, heat is conducted downward through the structure to the build plate. Consequently, the bottom layer (layer 2) is subjected to prolonged exposure to high temperatures, although these temperatures are lower than those experienced by the upper layers (layers 7 and 12). In contrast, the top section of the part (layer12) is subjected to high melting temperatures (above 1000 °C in average as seen in Figure 4) as heat accumulates with a longer resistive path to the build plate trajectory. The effects of these two distinct thermal history extremes — (*a*) prolonged low temperature duration and high thermal gradients from the cooling of the build plate, and (*b*) brief high temperature duration with lower thermal gradients — significantly influence both the microstructure and strength of the fabricated part.

CTE

Invar 36 samples obtained by EDM of cuboids manufactured using the LHWD were subjected to a CTE test. A total of 7 groups of coupons, these being a baseline (which was obtained from commercially available invar rod) and B0, BRP45, and BRP90 specimens in both the *XY* and *Z* orientations were subjected to a dilatometry analytical test. From these coupons, three samples were evaluated from both the vertical and horizontal direction. Additionally, three samples from the commercially stock material were EDM and tested as the baseline.

Figure 5 shows the averaged CTE of the test specimens. The figure displays that the printed samples have a similar CTE (1.5 to 3 um/m·°C range), and does not seem to depend on the printing orientation. In this work, CTE shows minor changes regardless of tool path orientations. Similar observations were made in LPBF printing in which the CTE is isotropic in 0, 45, and 90 build orientations [16]. The analysis

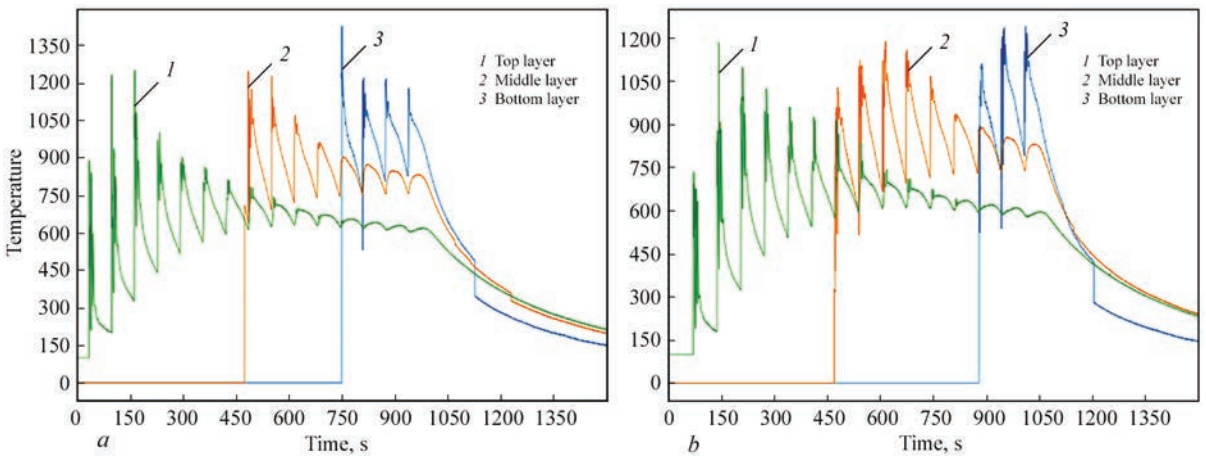

Figure 4. Temperature-time plot to identify the thermal behavior during the deposition and cool down of cuboids printed in *XY* (*a*), and *Z* orientations (*b*)

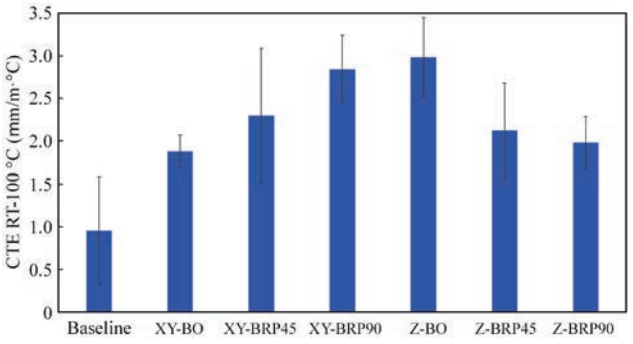

Figure 5. Average CTE results (0–100 °C) of the baseline and manufactured parts in *XY* and *Z* with B0, BRP45, and BRP90 orientations

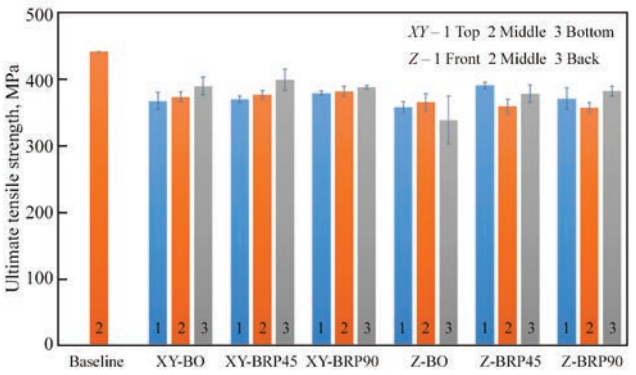

Figure 6. Tensile performance of the baseline and manufactured test specimen printed in *XY* and *Z* direction based on the B0, BRP45 and BRP90 orientations

of nickel on the printed samples at different locations is shown in Table 1. From the table, it is observed that the printed samples have a similar nickel content (about 35–36 %), a feature that governs their CTE. Additionally, the Curie temperature (T_c) values were also calculated from the results of the dilatometry test. It was here observed that the average T_c of the baseline samples was 280 ± 5 °C while the average T_c of the printed samples in the *XY* and *Z* orientation resulted in 236.67 ± 18.86 and 225 ± 20.41 °C, respectively. This indicates that the printed samples will exhibit higher CTE values at elevated temperatures, since they will reach out the curie temperature sooner. This performance can be associated with Figure 5, where the CTE of the baseline sample is lower compared to the printed samples. Since the acceptable CTE range for practical applications using wrought Invar 36 is below $2 \cdot 10^{-6}$ °C [26], from Figure 5 we can conclude that XY-B0, Z-BRP45, and Z-BRP90 are reasonable choices in terms of CTE.

Table 3. Summarized mechanical properties of baseline and 3D printed Invar 36 specimens

Sample name	Location	Averaged values		
		UTS, MPa	Yield strength, MPa	Elongation, %
Baseline	–	441.57	263.43	48.15
XY-B0	Top	374.49	209.19	30.92
	Middle	368.73	184.79	37.22
	Bottom	397.45	206.84	36.03
XY-BRP45	Top	361.25	175.36	45.77
	Middle	384.70	190.99	41.21
	Bottom	408.23	204.93	42.20
XY-BRP90	Top	380.55	191.71	42.78
	Middle	381.33	218.15	37.27
	Bottom	387.77	205.65	40.30
Z-B0	Front	357.83	175.99	43.38
	Middle	365.34	185.00	42.46
	Back	367.16	196.46	40.78
Z-BRP45	Front	390.52	194.70	36.78
	Middle	359.56	185.42	39.74
	Back	378.00	196.37	37.25
Z-BRP90	Front	370.59	187.76	35.59
	Middle	357.47	182.97	40.68
	Back	382.25	191.78	38.49

MECHANICAL PROPERTIES

Tensile tests were conducted on specimens obtained from two orientations i.e. *XY* and *Z*, and from three different locations; top, middle, and bottom (for the *XY* printing) and front, middle, and back (for the *Z* printing) as shown in Figure 6**.** These samples were taken from multi-layered build structures manufactured in B0, BRP45, and BRP90 directions for both orientations. The average UTS, YS, and % elongation of the Baseline and all printed samples are summarized in Table 3.

From Table 3, it is observed that the specimens built in the *Z* orientation have both lower UTS and YS values than those built in the *XY* orientation (by roughly 10 and 5 % respectively) but have similar elongation between the two printing orientations. Here, the averaged tensile strength of the *Z* and *XY* builds yielded a value of about 370 and 383 MPa, respectively. This difference could be associated with the anisotropic property-performance typically observed when printing on the Z-direction [27–31]. In the *XY* orientation builds, it is observed that the bottom samples showed a slightly superior strength than the samples from the middle and top. A mechanism associated with the smaller grain structure due to the thermal sink provided by the building plate. In contrast, the samples from the Z-build does not seem to show a clear trend. Table 3 shows that both printed builds resulted in inferior mechanical properties than the wrought Invar 36 material, similar to what other researchers have observed [32]. Fracture analysis was conducted on the surfaces of the tested tensile specimens using SEM, EDS, and digital microscopy. All the specimens in both orientations and all directional

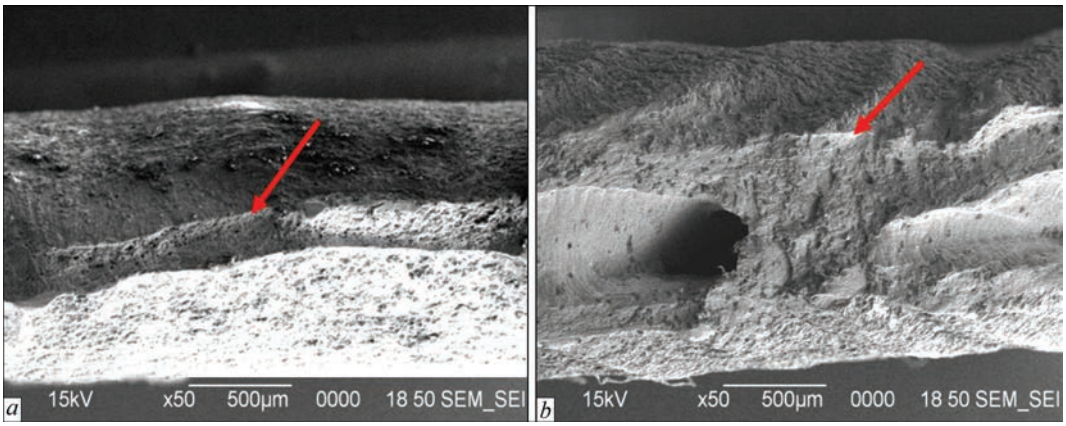

Figure 7. Fracture surface of the tested tensile specimen: *a* — Z-BRP45; *b* — XY-BRP90 displaying a ductile fracture profile

builds displayed a ductile fracture. The typical failure mechanism is evident in Figure 7 where the fracture surface(s) show necking back to the unaffected surfaces due to the elongation of the sample. The hardness tests were conducted on tensile samples and the results are summarized in Figure 8.

The figure shows that the specimens from the *Z* build yielded an average hardness *HRB* of 60.6, which is about 10 % lower than the average hardness (*HRB* 66.9) recorded on the *XY* specimens. These results appear to follow the trend observed on the tensile strength results. The figure also shows that specimens from both printed builds resulted in a hardness considerably lower than the recorded on the baseline. This difference as well as that observed on the tensile strength is associated to the thermal load-history induced on the parts during the printing process.

MICROSTRUCTURE ANALYSIS

XRD INVESTIGATION

The XRD investigations combined with the chemical analysis information, revealed that the main phase of the hybrid manufactured samples was based on an iron nickel phase (Fe0.66 Ni0.34). SEM/EDS investigations, reported below, indicate the presence of secondary phases. However, it was not possible to confirm the existence of a secondary phase using the Rigaku Miniflex XRD. Here, all the printed Invar samples showed similar diffraction peaks like the plot shown in Figure 9. This plot displays the top, middle, and bottom sections of the BRP90 sample in the *XY* orientation. Three diffraction peaks corresponding to the Fe0.66 Ni0.34 phase (cubic unit cell, $a = 3.604$ Å) can be observed at $2\theta = 43.47$, 50.58, and 74.55, corresponding to (111), (200), and (220) crystallographic planes, respectively. It must be noted, the other set of three diffraction peaks at $2\theta = 41.61$, 48.32, and 70.92, are due to the contamination of the X-ray tube in the Rigaku Miniflex, with a sputtered tungsten-base phase from the tungsten target (formed in an overused X-ray tube). The difference in peak height observed in top, middle, and bottom samples might be related to the samples' texture and grain preferential orientation, related to the printing and localized cooling conditions. The differences in texture among the top, middle, and bottom samples were confirmed by further light microscopy studies. Figure 10 shows the XRD spectra obtained from three samples prepared from the commercial Invar 36 bar. Here, the primary crystallographic phase is iron nickel, as well; however, the Fe0.65Ni0.35 (PDF 04-006-6665) index indicates a slight difference in the chemical composition compared to the printed Invar 36.

OPTICAL MICROSCOPY

The optical microscopy study was only performed on the *XY* samples to investigate the morphological aspects of the printed system across the height. The study indicates microstructural differences among the bottom, middle, and top locations, irrespective of the sample set. Typical grain features are shown in Figure 11 under a low magnification dark field. Here, the average grain size seems to increase from the bottom sample to the top sample. Elongated grains are observed in the bottom and middle sample, while the top sample shows equiaxed grain. The preferential orientation of the elongated grains might be related to the localized cooling conditions in the bottom and middle volumes of the printed Invar 36. The increase in grain

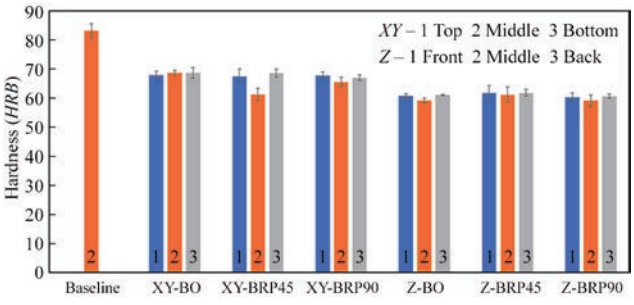

Figure 8. Rockwell hardness (*HRB*) performance of the baseline and manufactured test specimen printed in *XY* and *Z* with B0, BRP45, and BRP90 orientations

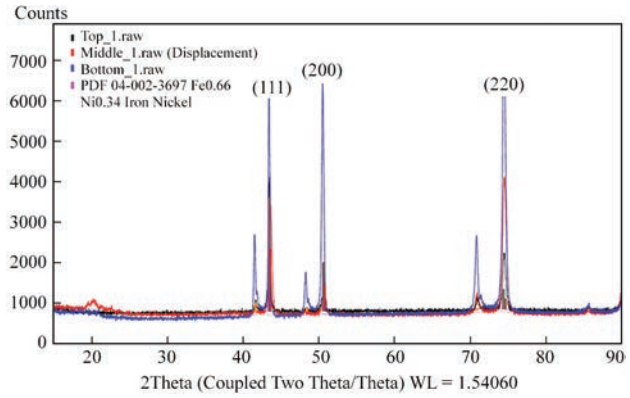

Figure 9. XRD spectra from top, middle, and bottom sections of XY-BRP90

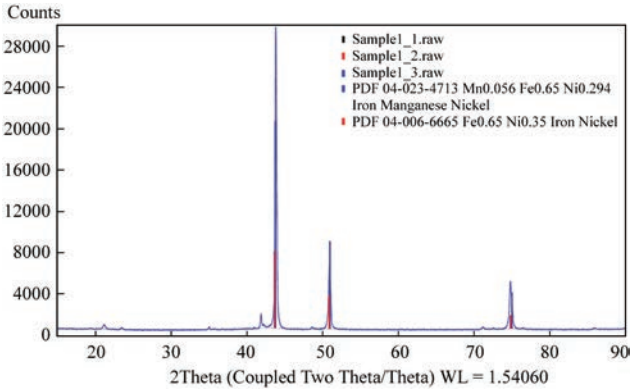

Figure 10. XRD spectra from commercially available Invar 36 baseline bar

size from the bottom to the top samples is highlighted on Figure 12 under a high magnification microscope.

The smaller grain size of the bottom sample, compared to the top one, might be explained by the fast-cooling conditions of the printed volume in contact with the build plate and the extended thermal history as shown by the infrared data. Figure 12 shows part of the laser track. The elongated grains of the bottom part grow perpendicular to the semicircular melt-pool boundary and toward the centerline of the melt pool, which is the hottest point of the molten pool. Due to the high thermal gradient in the direction orthogonal to the semicircular melt-pool boundary, epitaxial grain growth in this direction is the typical solidification mechanism that occurs in volumes of

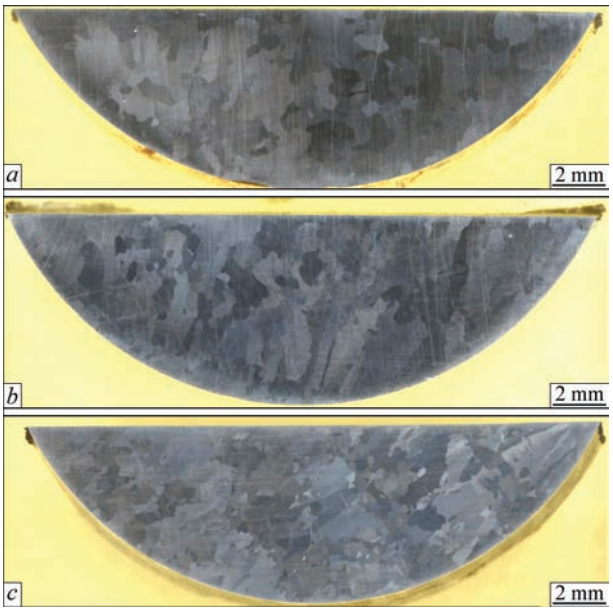

Figure 11. Dark field LM micrographs of the cross-sectioned top (*a*), middle (*b*), and (*c*) bottom of Bi0 sample printed in *XY* orientation

bottom and middle parts. It is interesting to note the presence of micro-porosity on the printed samples, a feature that was observed near the edges of the specimens. Previous studies on powder and wire DED have shown that mechanisms associated with gas and bubbles trapped in the pool contribute to the formation of pores [33, 34]. This clearly suggests that a further optimization on the printing parameters is required to minimize such defects.

SEM/EDS INVESTIGATION

Figure 13 shows the typical secondary electron micrographs collected from the printed samples. The SEM investigation confirms the grain size increase from bottom to the top of the printed Invar 36 samples. Also, the micron-scale porosity seems to increase from the bottom to the top of the sample. Grain size [18] and porosity variation [25], combined with the variation in the chemical composition (see below) could explain the variation in the coefficient of thermal expansion (CTE) in the as-printed Invar 36.

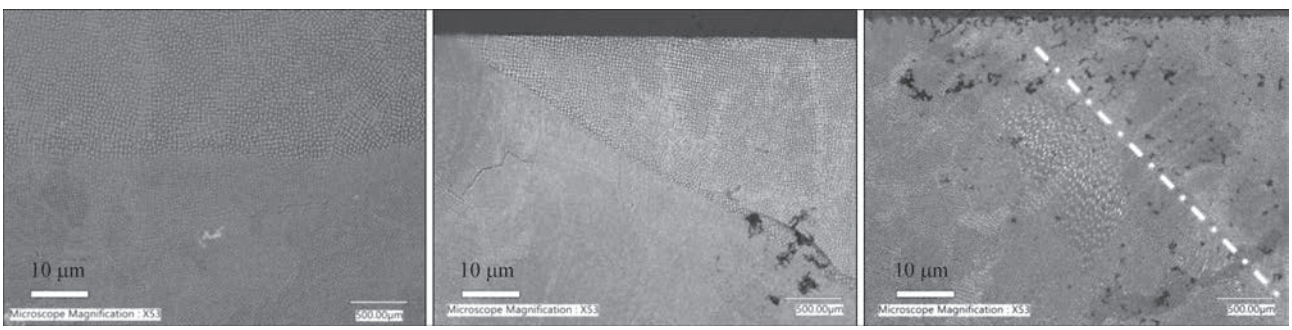

Figure 12. Typical bright field LM micrographs of the cross-sectioned top (*a*), middle (*b*) and bottom (*c*) volumes of Bi0 sample printed in *XY* orientation. Laser track in (*c*) indicated by dotted line

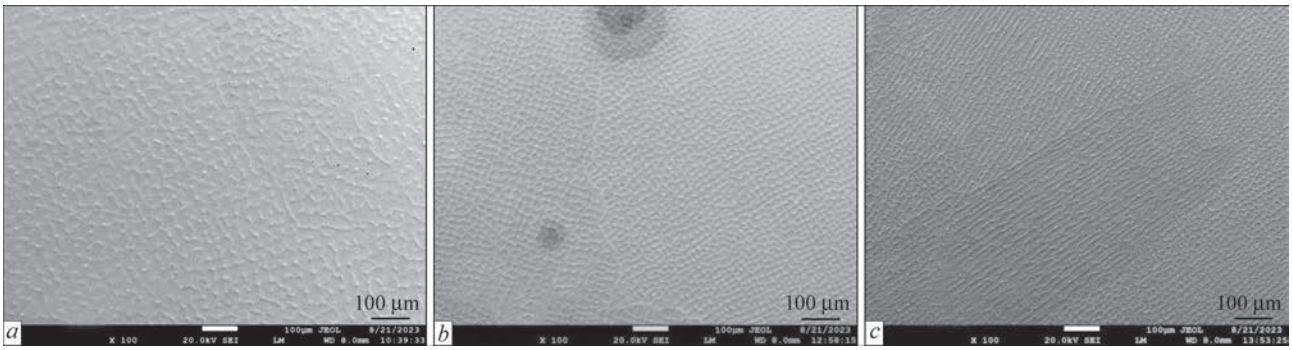

Figure 13. Secondary electron micrographs of the cross-sectioned XY-Bi0 sample top (*a*), middle (*b*) and bottom (*c*)

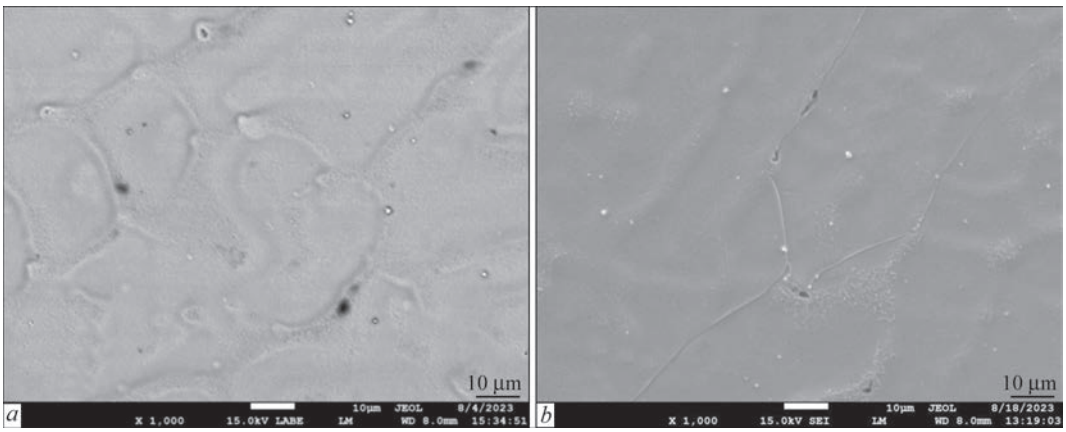

Figure 14. Representative SEM of the cross-sectioned samples: *a* — backscattered electron (BSE) micrograph of the XY-BRP90 specimen; *b* — secondary electron micrograph of the XY-BRP45 coupon

Figure 14 shows the representative backscattered electron (BSE) micrographs of the printed samples. For instance, the BSE contrast on the top sample collected from *XY* printed orientation (Figure 14, *a*), indicates the presence of at least two phases having different chemical (and very probably, crystallographic) content. Figure 14, *b* shows an electron micrograph of the bottom section of the XY sample, where elongated voids can be observed. The microscale voids dotting the crack path seem to be stress raisers for the applied stress.

Based on the EDS investigation, the chemical composition of all as-printed samples varies from the bottom to the top. A feature that could affect the mechanical and thermal properties of the printed coupons. This variation might be related to the change in printing conditions (printing parameters and printing environment), and to the presence of microvoids in the manufactured coupons. Figure 15, *a* shows the mean chemical composition of top, middle, and bottom volumes of a *XY* sample. The Fe content increases about 1.7 wt.% in between middle and top volumes, while

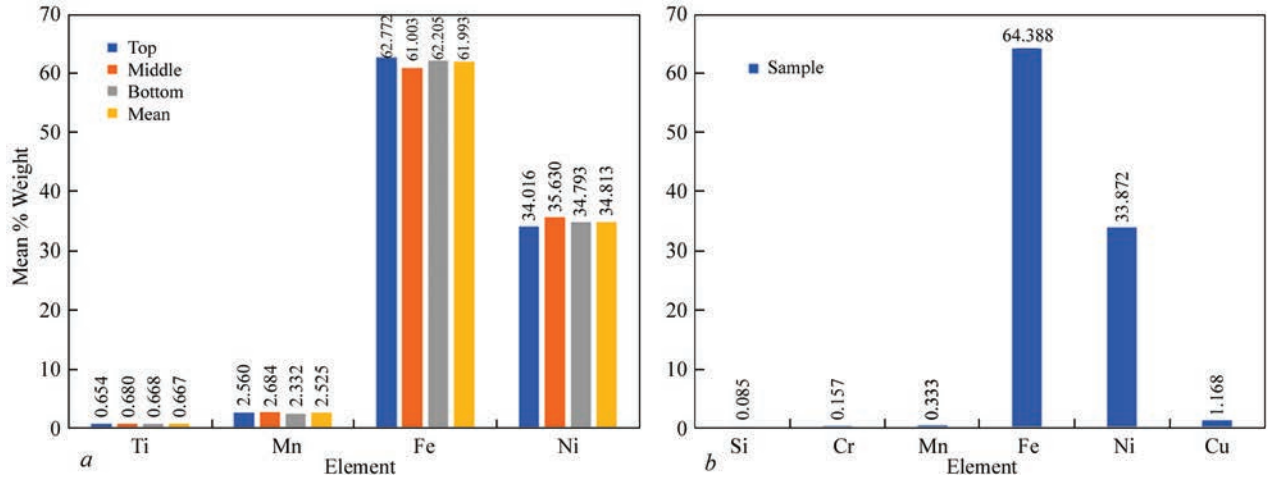

Figure 15. Chemical composition of top, middle, and bottom volumes of XY-BRP90, as determined by EDS investigation (*a*); chemical composition of commercially available Invar 36 rod, as measured in the present research (*b*)

Ni content decreases about 1.6 wt.%. This reduction in Ni content resulted in the higher CTE of printed parts. The Fe content in the hybrid manufactured Invar 36 sample is about 61.993 wt.%, while in the commercially available Invar 36 rod, the Fe content is about 64.388 wt.% (see Figure 15, *b*).

CONCLUSIONS

Test specimens manufactured using the Mazak LHWD hybrid system were studied in this work. The manufactured specimens were subjected to a series of mechanical and thermal tests to investigate their fundamental properties. The results showed that the printed parts exhibited a lower tensile and hardness performance than the commercially available material. Here, the samples obtained from the top section of the printed parts yielded higher mechanical properties than those extracted from the bottom; a feature associated to the heat sink performance provided by the building plate as well as to the larger thermal history to which the bottom sections were subjected to as recorded by an infrared camera. Indeed, an optical microscopy and SEM analysis revealed smaller crystal grains at the bottom of the printed samples than at the top. On the other hand, no clear distinction was observed on the coefficient of thermal expansion in terms of the printing location and manufacturing orientation. Here, although the printed samples resulted in a higher CTE than the commercially available Invar 36 stock material, their CTE values varied between 1.5 and 3 μm/m·°C. An ESD analysis showed that the printed samples yielded in average about 34 % Nickel, a percentage that could support their higher CTE. This work provides a preliminary study of DED printed Invar 36 as a feasible material for manufacturing low CTE composite tooling molds. Indeed, the incorporation of the hybrid technology will provide light-weight complex molds with tight dimensional requirements and surface finishes associated with typical subtracting CNC processes.

FUNDING ACKNOWLEDGEMENT

This material is based on research sponsored by Air Force Research Laboratory under Agreement Number FA8650-20-2-5700. The U.S. Government is authorized to reproduce and distribute reprints for Governmental purposes notwithstanding any copyright notation thereon.

This material is based upon work supported by the U.S. Department of Energy, Office of Energy Efficiency and Renewable Energy, Advanced Materials and Manufacturing Technologies Office (AMMTO) under contract number DE-AC05–00OR22725. The United States Government retains and the publisher, by accepting the article for publication, acknowledges that the United States Government retains a non-exclusive, paid-up, irrevocable, world-wide license to publish or reproduce the published form of this manuscript, or allow others to do so, for United States Government purposes. The Department of Energy will provide public access to these results of federally sponsored research in accordance with the DOE Public Access Plan (http://energy.gov/downloads/doe-public-access-plan).

We would like to highlight the support from the Murchison Chair at the University of Texas at El Paso, and the Friedman Chair at Youngstown State University.

DISCLAIMER

The views and conclusions contained herein are those of the authors and should not be interpreted as necessarily representing the official policies or endorsements, either expressed or implied, of Air Force Research Laboratory or the U.S. Government.

ACKNOWLEDGEMENT

This manuscript has been authored by UT-Battelle, LLC, under contract DE-AC05-00OR22725 with the US Department of Energy (DOE). The US government retains and the publisher, by accepting the article for publication, acknowledges that the US government retains a nonexclusive, paid-up, irrevocable, worldwide license to publish or reproduce the published form of this manuscript, or allow others to do so, for US government purposes. DOE will provide public access to these results of federally sponsored research in accordance with the DOE Public Access Plan.

REFERENCES

1. Acharya, S.S., Medicherla, V.R.R., Bapna, K. et al. (2021) Mixed ground state in Fe–Ni Invar alloys. *J. Alloys Compd.*, **863**, 158605.
2. Liu, H., Sun, Z., Wang, G. et al. (2016) Effect of aging on microstructures and properties of Mo-alloyed Fe–36Ni Invar alloy. *Materials Sci. and Eng.: A*, 654, 107–112.
3. Chen, C., Ma, B., Liu, B. et al. (2019) Refinement mechanism and physical properties of arc melted Invar alloy with different modifiers. *Mater. Chem. Phys.*, **227**, 138–147.
4. Ona, K., Sakaguchi, N., Ohno, H., Utsunomiya, S. (2020) The advanced super Invar alloys with zero thermal expansion for space telescopes. *Transac. of the Japan Soc. for Aeronautical and Space Sci., Aerospace Technology Japan*, **18**, 32–37.
5. Kim, B.G., Lee, D.G. (2009) The design of an optical sensor arrangement for the detection of oil contamination in an adhesively bonded structure of a liquefied natural gas (LNG) ship. *Meas. Sci. Technol.*, **20**, 065204.
6. He, G., Peng, X., Zhou, H. et al. (2023) Superior mechanical properties of Invar36 alloy lattices structures manufactured by laser powder bed fusion. *Materials*, **16**. DOI: https://doi.org/10.3390/ma16124433
7. Abbasi, S.M., Morakabati, M., Mahdavi, R., Momeni, A. (2015) Effect of microalloying additions on the hot ductility of cast FeNi36. *J. Alloys Compd.*, **639**, 602–610.
8. Martín-García, J.M., Portugal, R., Manssur, L.R.U. (2007) The Invar tensor package. *Comput. Phys. Commun.*, **177**, 640–648.
9. Wegener, T., Brenne, F., Fischer, A. et al. (2021) On the structural integrity of Fe–36Ni Invar alloy processed by selective laser melting. *Additive Manufacturing*, **37**, 101603.

10. Yakout, M., Elbestawi, M.A. (2020) Insights on laser additive manufacturing of Invar 36. In *Additive Manufacturing Applications for Metals and Composites*. IGI Global.
11. Sahoo, A., Medicherla, V.R.R. (2021) Fe–Ni Invar alloys: A review. *Materials Today: Proc.*, **43**, 2242–2244.
12. Kim, S.H., Choi, S.G., Choi, W.K. et al. (2014) Pulse electrochemical machining on Invar alloy: Optical microscopic/SEM and Non-contact 3D measurement study of surface analyses. *Appl. Surf. Sci.*, **314**, 822–831.
13. *Gil Del* Val, A., Cearsolo, X., Suarez, A. et al. (2023) Machinability characterization in end milling of Invar 36 fabricated by wire arc additive manufacturing. *J. of Materials Research and Technology*, **23**, 300–315.
14. Zhao, Y., Wu, A.P., Ren, J.L. et al. (2013) Temperature and force response characteristics of friction stir welding on Invar 36 alloy. *Sci. Technol. Weld. Joining*, ***18***, 232–238.
15. Jiang, Z., Chen, X., Li, H. et al. (2020) Grain refinement and laser energy distribution during laser oscillating welding of Invar alloy. *Mater. Des.*, **186**, 108195.
16. Huang, G., He, G., Liu, Y., Huang, K. (2024) Anisotropy of microstructure, mechanical properties and thermal expansion in Invar 36 alloy fabricated via laser powder bed fusion. *Additive Manufacturing*, **82**, 104025.
17. Rishmawi, I., Rogalsky, A., Vlasea, M. et al. (2022) The effects of heat treatment on tensile and thermal expansion behavior of laser powder-bed fusion Invar 36. *J. Mater. Eng. Perform.*, **31**, 9727–9739.
18. Huang, G., He, G., Peng, X. et al. (2024) Effect of processing parameters on the microstructure, mechanical properties and thermal expansion behavior of Invar 36 alloy manufactured by laser powder bed fusion. *Materials Sci. and Eng.: A*, **897**, 146329.
19. Ren, G., Cui, Z., Hao, X. et al. (2024) Effect of subgrain microstructure on the mechanical properties of Invar 36 specimens prepared by laser powder bed fusion. *J. Alloys Compd.*, **1004**, 175839.
20. Guo, H., Liu, D., Xu, M. et al. (2024) Preparation, characterization and composition optimization design of laser powder bed fusion continuously graded Invar 36/316L stainless steel alloys. *Mater. Charact.*, **209**, 113709.
21. Asgari, H., Salarian, M., Ma, H. et al. (2018) On thermal expansion behavior of Invar alloy fabricated by modulated laser powder bed fusion. *Mater. Des.*, **160**, 895–905.
22. Yakout, M., Elbestawi, M.A., Veldhuis, S.C. (2018) A study of thermal expansion coefficients and microstructure during selective laser melting of Invar 36 and stainless steel 316L. *Additive Manufacturing*, **24**, 405–418.
23. Garibaldi, M., Ashcroft, I., Simonelli, M., Hague, R. (2016) Metallurgy of high-silicon steel parts produced using selective laser melting. *Acta Mater.*, **110**, 207–216.
24. Tan, H., Wang, Y., Wang, G. et al. (2020) Investigation on microstructure and properties of laser solid formed low expansion Invar 36 alloy. *J. of Materials Research and Technology*, **9**, 5827–5839.
25. Huang, G., He, G., Gong, X. et al. (2024) Additive manufacturing of Invar 36 alloy. *J. of Materials Research and Technology*, **30**, 1241–1268.
26. Yang, Q., Wei, K., Yang, X. et al. (2020) Microstructures and unique low thermal expansion of Invar 36 alloy fabricated by selective laser melting. *Mater. Charact.*, **166**, 110409.
27. Carroll, B.E., Palmer, T.A., Beese, A.M. (2015) Anisotropic tensile behavior of Ti–6Al–4V components fabricated with directed energy deposition additive manufacturing. *Acta Mater.*, **87**, 309–320.
28. Wang, Z., Palmer, T.A., Beese, A.M. (2016) Effect of processing parameters on microstructure and tensile properties of austenitic stainless steel 304L made by directed energy deposition additive manufacturing. *Acta Mater.*, **110**, 226–235.
29. Tian, Y., McAllister, D., Colijn, H. et al. (2014) Rationalization of microstructure heterogeneity in Inconel 718 builds made by the direct laser additive manufacturing process. *Metall. Mater. Transact. A*, **45**, 4470–4483.
30. Sridharan, N., Gussev, M., Seibert, R. et al. (2016) Rationalization of anisotropic mechanical properties of Al-6061 fabricated using ultrasonic additive manufacturing. *Acta Mater.*, **117**, 228–237.
31. Wang, P., Tan, X., Nai, M.L.S. et al. (2016) Spatial and geometrical-based characterization of microstructure and microhardness for an electron beam melted Ti–6Al–4V component. *Mater. Des.*, **95**, 287–295.
32. Ngo, T.D., Kashani, A., Imbalzano, G. et al. (2018) Additive manufacturing (3D printing): A review of materials, methods, applications and challenges. *Composites Pt B*, **143**, 172–196.
33. Zhang, K., Chen, Y., Marussi, S. et al. (2024) Pore evolution mechanisms during directed energy deposition additive manufacturing. *Nat. Commun.*, **15**, 1715.
34. Yi, H., Yang, L., Jia, L. et al. (2024) Porosity in wire-arc directed energy deposition of aluminum alloys: Formation mechanisms, influencing factors and inhibition strategies. *Additive Manufacturing*, **84**, 104108.

ORCID

Bharat: 0000-0002-4580-6329
Mario Rodriguez: 0009-0000-9969-9656
Holly Martin: 0009-0007-0835-1680
Brian Vuksanovich: 0000-0002-7212-5801
Virgil Solomon: 0000-0003-2990-855X
Eric MacDonald: 0000-0002-9356-1223
Yousub Lee: 0000-0002-5563-0419
Thomas Feldhausen: 0000-0002-7311-5189

CONFLICT OF INTEREST

The Authors declare no conflict of interest

CORRESPONDING AUTHOR

Bharat Yelamanchi
Youngstown State University, OH USA 44555.
E-mail: byelamanchi@ysu.edu

SUGGESTED CITATION

Bharat Yelamanchi, Andrew Prokop, Coleman Buchanan, Aayush Alok, Mario Rodriguez, Jimena Morales, Holly Martin, Brian Vuksanovich, Virgil Solomon, Eric MacDonald, Yousub Lee, Thomas Feldhausen, Pedro Cortes (2024) Mechanical and thermal behavior of additively manufactured Invar 36 using a laser hot wire hybrid DED process. *The Paton Welding J.*, **11**, 3–13.
DOI: https://doi.org/10.37434/tpwj2024.11.01

JOURNAL HOME PAGE

https://patonpublishinghouse.com/eng/journals/tpwj

Received: 15.08.2024
Received in revised form: 04.10.2024
Accepted: 20.11.2024